9-27-2018

Momentum Flux Spectra of a Mountain Wave Event Over New Zealand

Katrina Bossert
Global Atmospheric Technologies and Science

David C. Fritts
Global Atmospheric Technologies and Science

Christopher J. Heale
Embry-Riddle Aeronautical University, HEALEC@erau.edu

Stephen D. Eckermann
U.S. Naval Research Laboratory

John M. C. Plane
University of Leeds

See next page for additional authors

Journal of Geophysical Research: Atmospheres

RESEARCH ARTICLE
10.1029/2018JD028319

Momentum Flux Spectra of a Mountain Wave Event Over New Zealand

Katrina Bossert[1], David C. Fritts[1], Christopher J. Heale[2], Stephen D. Eckermann[3], John M. C. Plane[4], Jonathan B. Snively[2], Bifford P. Williams[1], Iain M. Reid[5,6], Damian J. Murphy[7], Andrew J. Spargo[6], and Andrew D. MacKinnon[4]

[1]Global Atmospheric Technologies and Science (GATS), Inc., Boulder, CO, USA, [2]Department of Physical Sciences, Embry-Riddle Aeronautical University, Daytona Beach, FL, USA, [3]Space Science Division, U.S. Naval Research Laboratory, Washington, DC, USA, [4]School of Chemistry, University of Leeds, Leeds, UK, [5]ATRAD Pty Ltd, Thebarton, South Australia, Australia, [6]School of Physical Sciences, University of Adelaide, Adelaide, South Australia, Australia, [7]Department of Environment and Energy, Australian Antarctic Division, Kingston, Tasmania, Australia

This article is a companion to Fritts et al. (2018) https://doi.org/10.1029/2017JD028250.

Key Points:
- A multiscale spectrum of mountain waves was observed during a mesospheric mountain wave event over New Zealand
- Temperatures of the mountain waves were derived using sodium density mixing ratios
- Average momentum fluxes associated with observed mountain waves were large compared to zonal means

Supporting Information:
- Figure S1
- Data Set S1
- Data Set S2
- Data Set S3
- Data Set S4
- Data Set S5
- Data Set S6
- Data Set S7

Correspondence to:
K. Bossert,
k.bossert@gats-inc.com

Citation:
Bossert, K., Fritts, D. C., Heale, C. J., Eckermann, S. D., Plane, J. M. C., Snively, J. B., et al. (2018). Momentum flux spectra of a mountain wave event over New Zealand. *Journal of Geophysical Research: Atmospheres*, *123*, 9980–9991. https://doi.org/10.1029/2018JD028319

Received 17 JAN 2018
Accepted 5 JUL 2018
Accepted article online 13 JUL 2018
Published online 17 SEP 2018

Abstract During the Deep Propagating Gravity Wave Experiment (DEEPWAVE) 13 July 2014 research flight over the South Island of New Zealand, a multiscale spectrum of mountain waves (MWs) was observed. High-resolution measurements of sodium densities were available from ~70 to 100 km for the duration of this flight. A comprehensive technique is presented for obtaining temperature perturbations, T', from sodium mixing ratios over a range of altitudes, and these T' were used to calculate the momentum flux (MF) spectra with respect to horizontal wavelengths, λ_H, for each flight segment. Spectral analysis revealed MWs with spectral power centered at λ_H of ~80, 120, and 220 km. The temperature amplitudes of these MWs varied between the four cross-mountain flight legs occurring between 6:10UT and 9:10UT. The average spectral T' amplitudes near 80 km in altitude ranged from 7–13 K for the 220 km λ_H MW and 4–8 K for the smaller λ_H MWs. These amplitudes decayed significantly up to 90 km, where a critical level for MWs was present. The average MF per unit mass near 80 km in altitude ranged from ~13 to 60 m^2/s^2 across the varying spectra over the duration of the research flight and decayed to ~0 by 88 km in altitude. These MFs are large compared to zonal means and highlight the importance of MWs in the momentum budget of the mesosphere and lower thermosphere at times when they reach these altitudes.

1. Introduction

Gravity waves (GWs) have been known for many years to play major roles in the dynamics and structure of the atmosphere from the Earth's surface into the mesosphere and lower thermosphere (MLT). A key role is the transport and deposition of momentum from sources at lower altitudes to regions of dissipation at higher altitudes. Momentum flux (MF) divergence causes flow accelerations in the direction of horizontal GW propagation, and the cumulative effects in the MLT are decelerations and even reversals of the zonal flow in both hemispheres and an induced residual circulation from the summer to winter hemisphere near the mesopause (Fritts & Alexander, 2003; Garcia & Solomon, 1985; Holton, 1982, 1984). Orography is a major source of GW generation, and orographic GWs are a key component in parameterizations used in global circulation and climate models (Alexander et al., 2010; Kim et al., 2003). Multiple satellite observations have demonstrated GW *hot spot* regions in the stratosphere over major orography, suggesting the significant role that mountain waves (MWs) play at these higher altitudes (Eckermann & Preusse, 1999; Gong et al., 2012; Hoffmann et al., 2013; Jiang et al., 2005; McLandress et al., 2000; Wu et al., 2006).

The Deep Propagating Gravity Wave Experiment (DEEPWAVE) observed GWs in the vicinity of an orographic GW hot spot over the South Island of New Zealand during June–July 2014 (Fritts et al., 2016). The National Center for Atmospheric Research/National Science Foundation (NCAR/NSF) Gulfstream V (GV) aircraft flew 25 research flights (RFs) out of Christchurch, NZ. Onboard GV instruments used during this campaign included both Rayleigh and sodium (Na) lidars allowing for measurements of the stratosphere and MLT, and an advanced mesospheric temperature mapper (AMTM), which provided temperatures derived from OH airglow emissions centered near ~87 km. Additionally, flight-level data were collected by in situ instrumentation. Through these campaign measurements, multiple MWs were observed throughout the atmosphere, and a number of these have been analyzed to date (Bossert et al., 2015, 2017; Bramberger

et al., 2017; Eckermann et al., 2016; Fritts et al., 2016; Kruse et al., 2016; Pautet et al., 2016; Smith & Kruse, 2017). This paper focuses on the multiscale MW event on 13 July 2014 observed from the GV RF, and calculations of its changing MF spectra over a range of altitudes and spatial regions. These calculations are performed using a presented technique for obtaining temperatures from mixing ratios associated with significant sodium density perturbations on the lower side of the sodium layer.

2. Measurements

During the RF on 13 July 2014, the sodium lidar was run in a special high-resolution mode that provided sodium density measurements at 1-s sampling using one frequency; however, this nonstandard single-frequency measurement configuration prohibited the derivation of temperatures provided by the standard two laser frequency measurements. These high-resolution measurements allowed for the observation of small-scale secondary GWs within the sodium layer with horizontal wavelengths $\lambda_H < 40$ km along the flight track (Bossert et al., 2017), as well as a $\lambda_H \sim 200$–240 km MW, which persisted for the entire flight duration (Bossert et al., 2015). There were four flight passes during the RF across the South Island, and these all traversed the highest peak, Mt. Cook. These flight passes took place between 6:10UT and 9:10UT, with sodium lidar data acquisition beginning at 6:20UT.

The data used in this study were filtered using a boxcar moving average window over 1.8 km (6 altitude bins) and 15 s (15 temporal bins), the latter corresponding to an along-track horizontal resolution of ~3.6 km given a mean GV cruise speed of 240 m/s. During the second and third passes, the lidar data were affected by intermittent problems with the laser's locking to the sodium line. In order to use all of the data, a temporal low-pass filter was applied to remove locking-related anomalies from the data series while retaining GW horizontal wavelengths of $\lambda_H \sim 30$ km and larger. The applied filter had a passband of 100 s (~24 km along track) and a stopband of 50 s (~12 km along track).

3. Temperature and MF Measurements and Validation

Several methods are available to infer GW-induced temperature perturbations diagnostically from observed GW-induced sodium density perturbations. Sodium density perturbations have previously been used to calculate temperature perturbations associated with GWs (Bossert et al., 2014; Shelton et al., 1980; Swenson & Gardner, 1998), and sodium lidars have also been previously used to calculate MFs associated with GWs (Acott et al., 2011; Gardner & Liu, 2007). Assuming hydrostatic GWs and purely vertical and linear gradients in background temperatures and sodium densities, GW-induced perturbations in temperature can be derived from sodium density perturbations using parcel-advection methods (see Eckermann et al., 1998). The diagnostic relation relating sodium density perturbations (assuming conservation of the sodium mixing ratio and potential temperature following air motions) is given in equation (1),

$$\rho'_{\mathrm{Na}} = \left[\frac{\overline{\rho}_{\mathrm{Na}}}{\gamma H} + \frac{\partial \overline{\rho}_{\mathrm{Na}}}{\partial z}\right]\left(\frac{gT'}{N^2\overline{T}}\right) \tag{1}$$

where ρ'_{Na} is the sodium density perturbation, $\overline{\rho}_{\mathrm{Na}}$ is the background sodium density, T' is the temperature perturbation, $\overline{T}$ is the background temperature, γ is the ratio of specific heats, g is the gravitational acceleration, N is the background buoyancy frequency in rad/s, and H is the pressure scale height.

The GW-induced T' can also be calculated by using the observed vertical displacement of Na mixing-ratio isopleths. This approach was used as an approximate calculation for T' for the large scale ~240 km MW present during the 13 July 2014 RF in Bossert et al. (2015), as well as the ~40 km MW observed over the Auckland Islands the following day (Eckermann et al., 2016). In the absence of chemistry, the mixing ratio of any minor constituent is conserved under adiabatic isobaric advection. In such cases, the observed vertical displacement of isopleths of tracer mixing ratio from their undisturbed equilibrium altitudes, Δz_{mix}, provides a direct measurement of the GW-induced vertical displacement perturbation. The resulting temperature perturbation T' due to adiabatic expansion and compression of the air parcel during this vertical advection is given by equation (2),

Table 1
Variables Commonly Referred to in This Paper

Parameter	Description
T'	gravity wave temperature amplitude
$\overline{T}$	mean background temperature
g	gravitational acceleration
λ_H	horizontal wavelength
ρ'_{Na}	sodium density perturbation
N	buoyancy frequency
$\overline{\rho}_{Na}$	mean sodium density
γ	ratio of specific heats
Γ	adiabatic lapse rate
R	ideal gas constant
M	average atmospheric molecular weight
$k_H = 2\pi/\lambda_H$	horizontal wavenumber
$m = 2\pi/\lambda_z$	vertical wavenumber
u_H'	horizontal wind perturbation in GW propagation direction
U_H	horizontal wind in GW propagation direction
$H = R\overline{T}(z)/Mg$	pressure scale height

$$T' = -\Delta z_{mix}\left(\Gamma + \frac{dT}{dz}\right) \quad (2)$$

where Γ is the adiabatic lapse rate 9.5 K/km and $\frac{dT}{dz}$ is the background temperature gradient. Table 1 gives an overview of the variables used in equations (1) and (2) as well as those used later in this paper. Equation (1) is more accurate for cases in which perturbations are observed within the sodium layer with smaller parcel altitude displacement. Equation (2) works better for larger amplitude waves since Δz_{mix} is quantified directly from observed mixing ratios. Both methods also assume approximate hydrostatic equilibrium and adiabatic motion, which may not always be strictly valid for large-amplitude and short-scale GWs. For the observed GWs on 13 July, the amplitudes of the MWs on the bottom side of the layer were large enough to significantly perturb sodium densities from the layer. In this case, it is difficult to assess a relative background sodium density with respect to observed sodium density perturbations; thus, equation (1) would not be applicable. Therefore, equation (2) is used for the subsequent temperature analysis.

3.1. Temperature Calculations From Modeled Sodium Density

A previous 2-D simulation of the observed λ_H ~240 km MW during the 13 July 2014 event by Heale et al. (2017) provided GW-induced perturbations in both temperature and sodium densities. Sodium densities from this simulation were also published and used for the investigation of arising secondary features associated with primary MW breaking (Bossert et al., 2017). The fields from this simulation allow for sodium mixing ratio perturbations to be calculated and converted into temperature perturbations using equation (2), which can then be compared and objectively validated against the directly simulated temperature perturbations from the model. Sodium mixing ratios were derived using background densities from the Navy Global Environmental Model (NAVGEM). The calculation for the sodium mixing ratio is given in equation (3),

$$R_{Na} = \frac{\rho_{Na}(z)T(z)}{\rho_{atm}(z_o)T(z_o)\exp\left[-\int_{z_o}^{z}\frac{dz}{H(z)}\right]} \quad (3)$$

where ρ_{atm} is the atmospheric background density. For the purposes of mixing ratio calculations in this paper, which use the background atmospheric density from NAVGEM reanalysis, equation (3) simplifies to $R_{Na} = \rho_{Na}(z)/\rho_{atm}(z)$. From these mixing ratios, T' was calculated using equation (2) and the background temperature profile from NAVGEM. Figure 1 shows the modeled T' and modeled sodium densities over a region of the 240 km MW with breaking and associated features occurring and corresponding T' calculated from the mixing ratio displacements for 49 different mixing ratio isopleths. As can be seen from Figures 1a

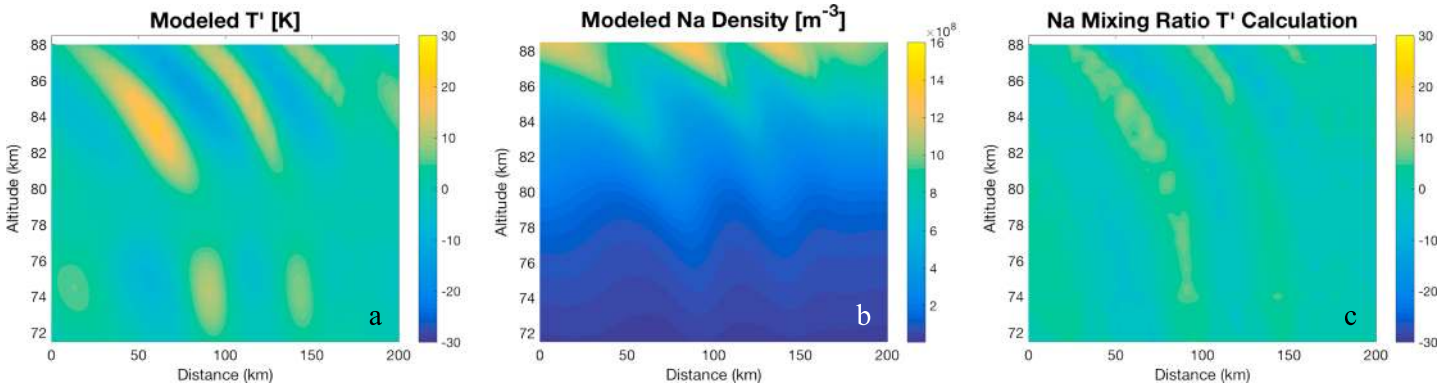

Figure 1. (a) The modeled T' from Heale et al. (2017). (b) The associated sodium densities from this model. (c) The T' calculated from the sodium mixing ratio calculated using equations (2) and (3).

and 1c, there is a reasonable match between the actual T' and calculated T'. The method is only applicable to adiabatic motions and will not provide a reliable estimate under conditions where horizontal advection is significant and diabatic motions are dominant. Additionally, because the method provides an average T' over an entire parcel displacement, when a parcel is displaced through a region of temperature fluctuations that are smaller in vertical scale than the overall parcel displacement, these fluctuations will not be resolved. This is apparent in the modeled data, as there is a small region of evanescence between 77 and 79 km evident in Figure 1a, and this is not resolved in the mixing ratio calculated temperatures shown in Figure 1c. The model comparisons in Figure 1 demonstrate that the calculation of T' from mixing ratios as would be calculated with sodium density measurements provides an estimate on MW T' amplitudes spatially and vertically in the absence of chemistry, which allows for estimates of MF when no other high-resolution direct methods of temperature measurement are available.

3.2. Influences of Sodium Chemistry

In order to test the chemical response of the Na layer to wave-driven oscillations in temperature, pressure, and the mixing ratios of minor constituents, we employed a full time-resolved model of Na chemistry. The 1-D model is essentially that described by Plane (2004), with recent updates to the rate coefficients of some reactions, which were remeasured in the laboratory (Gómez-Martín et al., 2016; Gómez-Martín et al., 2017). The 12 neutral reactions, 10 ion-molecule reactions, and 5 photochemical reactions are listed in Table 2. Na, Na^+, NaOH, and $NaHCO_3$ are treated explicitly in the model, and the minor species (NaO, NaO_2, NaO^+, $Na^+.N_2$, and $Na^+.CO_2$) are assumed to be in chemical steady state (Plane, 2004).

Table 2
Neutral and Ionic Gas-Phase Reactions in the Sodium Model

Number	Reaction	Rate Coefficient[a]
	Neutral chemistry	
R1	$Na + O_3 \rightarrow NaO + O_2$	$1.1 \times 10^{-9} \exp(-116/T)$
R2	$NaO + O \rightarrow Na + O_2$	$2.2 \times 10^{-10} (T/200)^{1/2}$
R3	$NaO + O_3 \rightarrow Na + 2O_2$	$3.2 \times 10^{-10} (\exp(-550/T)$
R4	$NaO + H_2 \rightarrow NaOH + H$	4.9×10^{-12}
R5	$NaO + CO \rightarrow Na + CO_2$	9.0×10^{-11}
R6	$NaO + H_2O \rightarrow NaOH + OH$	$5.1 \times 10^{-10} \exp(-240/T)$
R7	$NaOH + H \rightarrow Na + H_2O$	3.9×10^{-11}
R8	$NaOH + CO_2 (+M) \rightarrow NaHCO_3$	$1.2 \times 10^{-27} (T/200)^{-4.12}$
R9	$NaHCO_3 + H \rightarrow Na + H_2CO_3$	$1.84 \times 10^{-13} T^{0.777} \exp(-1014/T)$
R10	$Na + O_2 (+M) \rightarrow NaO_2$	$5.0 \times 10^{-30} (T/200)^{-1.22}$
R11	$NaO_2 + O \rightarrow NaO + O_2$	$5.0 \times 10^{-10} \exp(-940/T)$
R12	$2NaHCO_3 (+M) \rightarrow$ dimer	$8.8 \times 10^{-10} (T/200\ \mathrm{K})^{-0.23}$
	Ion-molecule Chemistry	
R20	$Na + O_2^+ \rightarrow Na^+ + O_2$	2.7×10^{-9}
R21	$Na + NO^+ \rightarrow Na^+ + NO$	8.0×10^{-10}
R22	$Na^+ + N_2 (+M) \rightarrow Na.N_2^+$	$4.8 \times 10^{-30} (T/200)^{-2.2}$
R23	$Na^+ + CO_2 (+M) \rightarrow Na.CO_2^+$	$3.7 \times 10^{-29} (T/200)^{-2.9}$
R24	$Na.N_2^+ + X \rightarrow Na.X^+ + N_2$ (X = CO_2, H_2O)	6×10^{-10}
R25	$Na.N_2^+ + O \rightarrow NaO^+ + N_2$	4×10^{-10}
R26	$NaO^+ + O \rightarrow Na^+ + O_2$	1×10^{-11}
R27	$Na.O^+ + N_2 \rightarrow Na.N_2^+ + O$	1×10^{-12}
R28	$Na.O^+ + O_2 \rightarrow Na^+ + O_3$	5×10^{-12}
R29	$Na.Y^+ + e^- \rightarrow Na + Y$ (Y = N_2, CO_2, H_2O, O)	$1 \times 10^{-6} (T/200)^{-1/2}$
R30	$Na^+ + e^- \rightarrow Na + h\nu$	$3.9 \times 10^{-12} (T/200)^{-0.74}$
	Photochemical reactions	
R31	$NaO + h\nu \rightarrow Na + O$	5.5×10^{-2}
R32	$NaO_2 + h\nu \rightarrow Na + O_2$	1.9×10^{-2}
R33	$NaOH + h\nu \rightarrow Na + OH$	1.8×10^{-2}
R34	$NaHCO_3 + h\nu \rightarrow Na + HCO_3$	1.3×10^{-4}
R35	$Na + h\nu \rightarrow Na^+ + e^-$	2×10^{-5}

[a]Units: unimolecular, s^{-1}; bimolecular, $cm^3 \cdot molecule^{-1} \cdot s^{-1}$; termolecular, $cm^6 \cdot molecule^{-2} \cdot s^{-1}$. Rate coefficients are from Plane (2004), apart from R4, R5, R6, and R8 from Gómez-Martín et al. (2016), R7 from Gómez-Martín et al. (2017), and R30, which is calculated by Badnell (2006).

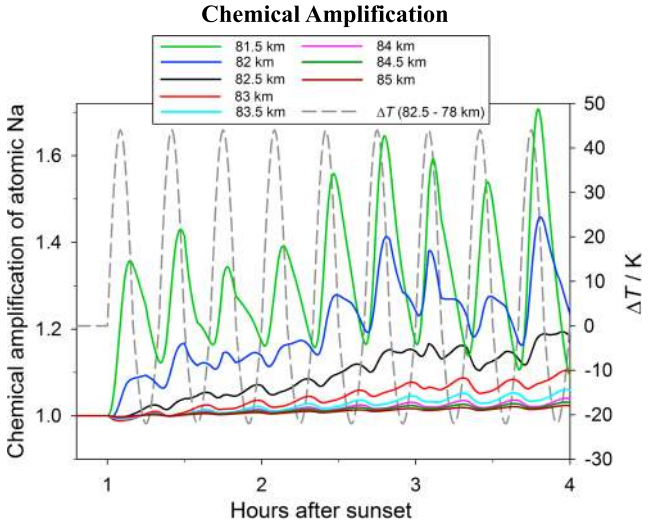

Figure 2. The chemical amplification factor (CAF) of atomic Na over 4 hr, for a wave period of 20 min. The black line shows the CAF when the Na vmr before the wave is 1.1×10^{-12}, which is at 82.5 km. The wave then displaces the air parcel down to 78 km, and up to 84.8 km (i.e., approximately 50% of the downward displacement). The resulting oscillation of the air parcel temperature is shown with the dashed grey line (right-hand ordinate axis). The CAFs for air parcels starting at other altitudes between 81.5 and 85 km, and displaced down to 78 km, are also shown in the figure.

The model was run under midlatitude conditions where all the minor atmospheric constituents, which control the Na chemistry (O_3, O, H, NO^+, O_2^+, and electrons), vary diurnally. A time step of 30 s was used. One hour after sunset the wave was turned on with a period of 20 min. In order to examine the effect of wave-driven chemistry on the underside of the layer consistent with the DEEPWAVE observations, we considered vertical displacements from mean heights between 81.5 and 85 km down to 78 km. The upward excursions were set to be 50% of the downward displacements due to strong constraints on the wave amplitude approaching a critical level at ~90 km.

The model was used to determine the chemical amplification factor (CAF) of atomic Na, defined as the Na vmr in an air parcel when it is displaced by the wave and full chemistry operates, divided by the Na vmr when chemistry is turned off and Na is treated as an inert tracer. Figure 2 illustrates how the CAF varies over 4 hr for the wave period of 20 min. The CAF is largest, up to 1.6, starting from a mean height of 81.5 km. This is where the Na vmr is very small (4.8×10^{-14}) at the base of the layer, and there is a very large reservoir of $NaHCO_3$. This reservoir species is converted into Na via reaction R9 (Table 2), which has a significant activation energy and thus produces Na rapidly due to adiabatic heating of the air parcel during the downward excursion. During the subsequent upward excursion, the CAF decreases as the temperature falls, though the CAF does not return to 1. This is because of nonlinear processes in the model; the third-order reactions R8, R10, and R12; and the smaller upward wave excursion.

At higher mean altitudes, the ratio of Na to $NaHCO_3$ increases rapidly, and so the CAF is essentially unity starting from a mean height of 85 km (Figure 2). At a mean height of 82.5 km, where the Na vmr is 1.1×10^{-12} and thus detectable by the airborne lidar operating at high time resolution, the CAF is less than 1.2.

3.3. Temperature Calculations From Measured Sodium Densities

Given the potential for mixing ratios to provide an estimate of GW T', they are used here for the calculations of T' associated with the multiple scales of MWs observed from the GV on 13 July 2014. Although the mixing ratios have been used previously for rough temperature estimates (Bossert et al., 2015; Eckermann et al., 2016), the analysis presented here corrects for chemical influences on the bottom side of the layer and investigates changes in temperature perturbation estimates with altitude. Additionally, the data presented here have been filtered using a low-pass filter instead of the long temporal boxcar averaging which was previously applied in Bossert et al. (2015). This allows for a more precise assessment of the mixing ratio perturbations and temperature amplitudes due to $\lambda_H < 100$ km. The mixing ratios calculated using equation (3) for the four flight segments across the South Island are shown in Figure 3. For the T' calculation, mixing ratios are calculated along 27 mixing ratio isopleths with average altitudes ranging from 79 to 89 km. The average altitude of each isopleth is used for the altitude of the calculated T' from equation (2). A correction factor accounting for the CAF shown in Figure 2 is then applied to the calculated T'. Correction factors plotted over a range of mixing ratios are shown in Figure 4. T' amplitudes are divided by the correction factors for each mixing ratio isopleth. Figure 5a shows the mixing ratio contours with one highlighted in red, which corresponds to an average altitude of 81.5 km. The corresponding temperature perturbations for this contour are shown in Figure 5b in red, and the corrected temperature perturbations accounting for the CAF are shown in black. The calculated temperature perturbations for each mixing ratio contour during the second pass are shown in Figure 5c. The calculated T' from mixing ratio contours for each pass are shown in Figure 6. The background $d\overline{T}/dz$ used in equation (2) was obtained from NAVGEM reanalysis (Eckermann et al., 2018), reinterpolated onto a constant geometric height grid for the 13 July 2014 flight. The temperature profile was the average of all reanalysis grid points within a circular region centered near Mt. Cook with a 600 km great circle radius, and for times from 0600–0900 UTC. These temperatures are shown in Figure 7.

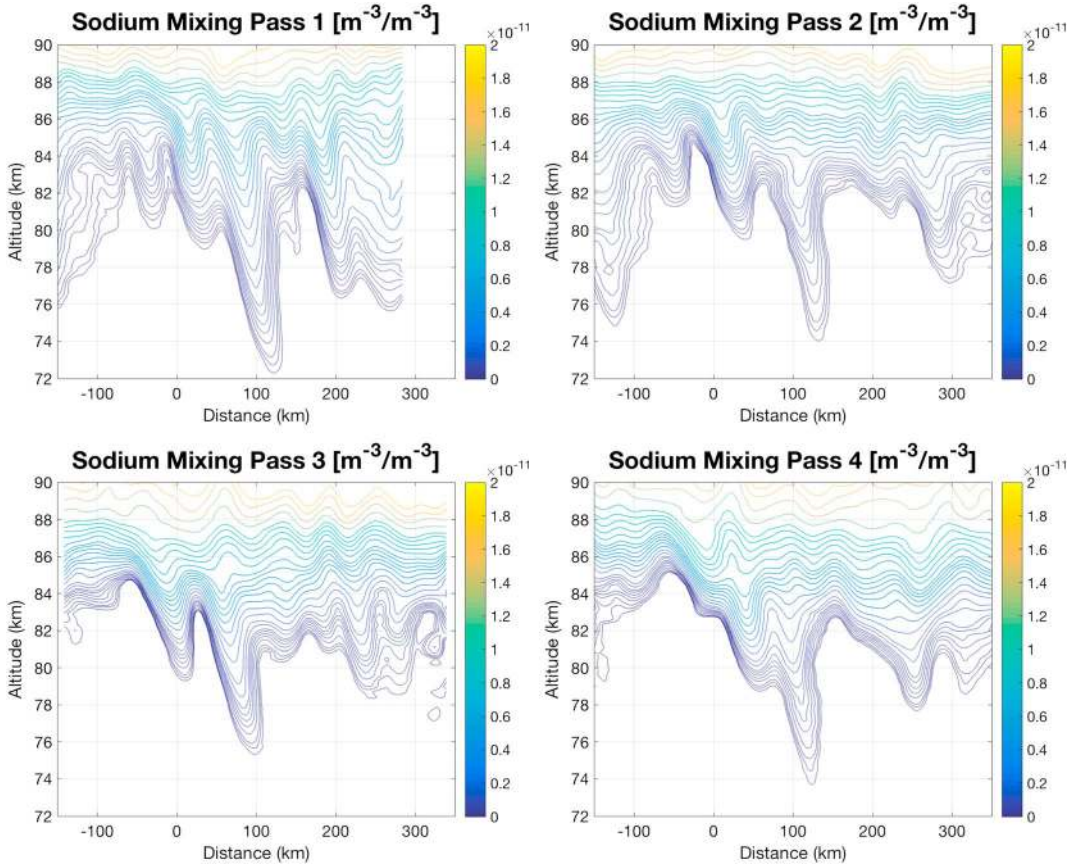

Figure 3. Sodium mixing ratio contours for all four passes calculated from observations using equation (3).

The T' given in Figure 6 reveal a superposition of multiple GWs with a range of different λ_H. In order to estimate the T' for each specific GW present, a fast Fourier transform (FFT) is applied to the along-track data at any given height, which provides a spectral amplitude for each transect. For each pass, data were zero-padded to length of 4,000 km. To reduce FFT sidelobes, data for the first and last 24 km were smoothed to a value of zero. The resulting spectral amplitudes are given in Figure 8. The FFT for each pass reveals spectral power centered around λ_H ~ 220, 120, and 80 km, with the spectral power being most significant on the first and second passes. The λ_H are consistent with observations at the flight level of the GV, and stratospheric lidar observations of MWs (Fritts et al., 2018), suggesting that these observed wavelengths are likely associated with MWs. As expected for MWs, all amplitudes for the λ_H ~ 220, 120, and 80 km decay upon approach to the MW critical level near 90 km. However, we also note that there may be contributions from GWs, which are not MWs. For example, scales of $\lambda_H < 60$ km are observed during each transect, which persist or arise near the critical level, indicating a nonzero phase speed. Additionally, in these nonMW cases, it is difficult to predict the associated phase speed, orientation, and thus, related MF. As demonstrated by the FFT plots, there is variation in MW amplitudes between each pass, and variation in the amplitudes between different λ_H, which is expected as forcing conditions have variation in time, and varying λ_H will have different responses to atmospheric fluctuations during upward propagation. Additionally, differences in dissipation can occur based on the initial amplitude of the wave and the

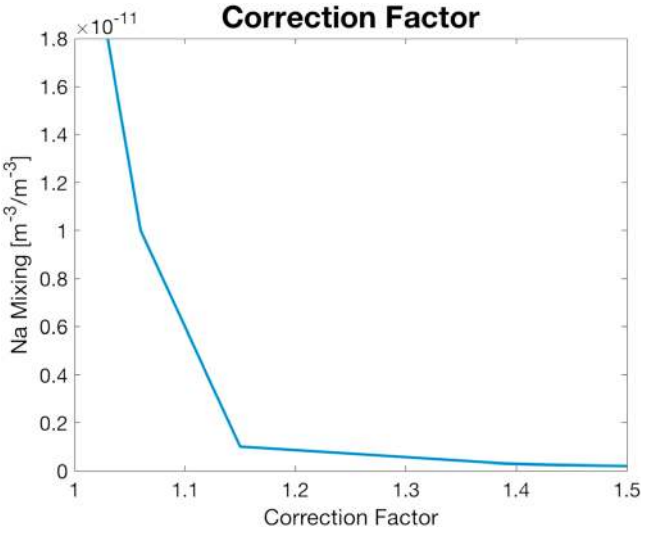

Figure 4. The correction factor obtained from Figure 2 and applied to the T' calculated from sodium mixing ratio displacements.

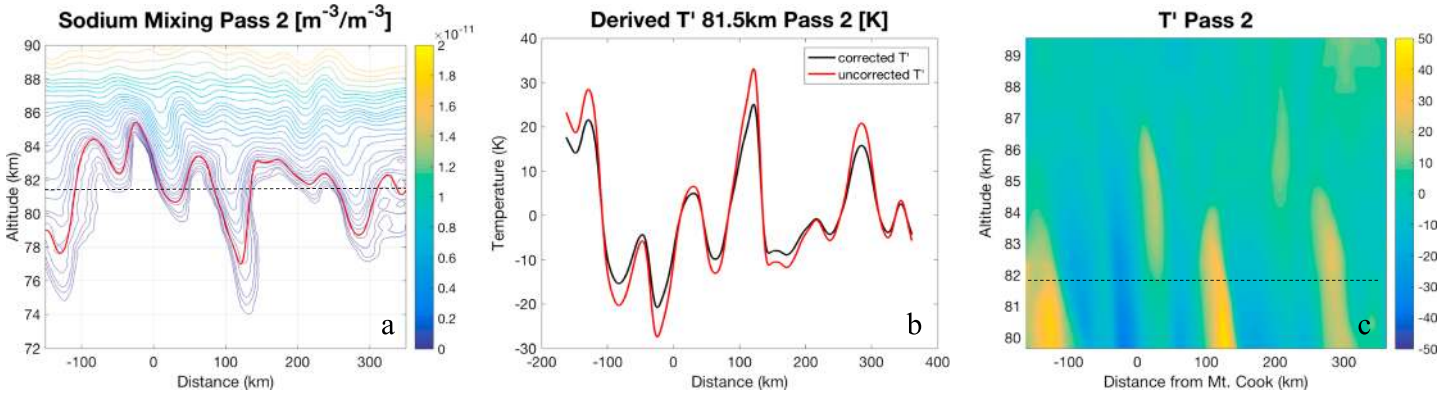

Figure 5. (a) Sodium mixing ratio contours for the second pass with a selected contour highlighted in red and the corresponding mean altitude of the contour shown by the black dotted line. (b) The corresponding T' derived from this contour using equation (2) in red, and the T' corrected for chemical amplification in black. (c) The corrected T' derived for each contour, and the black dotted line corresponds to the altitude for the temperature perturbations given in plot (b).

horizontal wavelength, as breaking is tied to multiple aspects of the GW and occurs upon approach to the critical level (Andreassen et al., 1998). The average spectral T' near 80 km in altitude varied from 7 to 13 K for the 220 km λ_H MW between each pass and ranged from 4 to 8 K for the smaller λ_H MWs for each pass. The λ_H and corresponding spectral average T' shown in Figure 8 are used to calculate MF spectra, which is discussed in the following section.

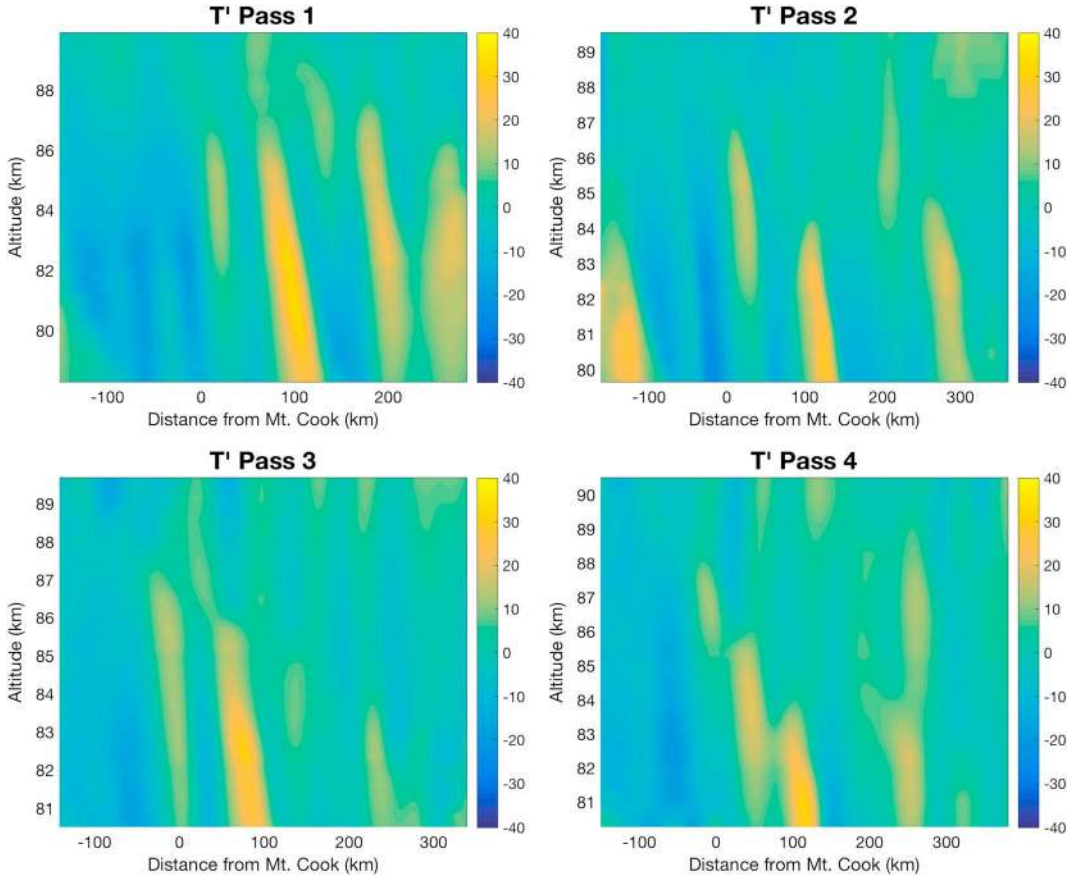

Figure 6. Calculated T' for each contour shown in Figure 2 using equation (2).

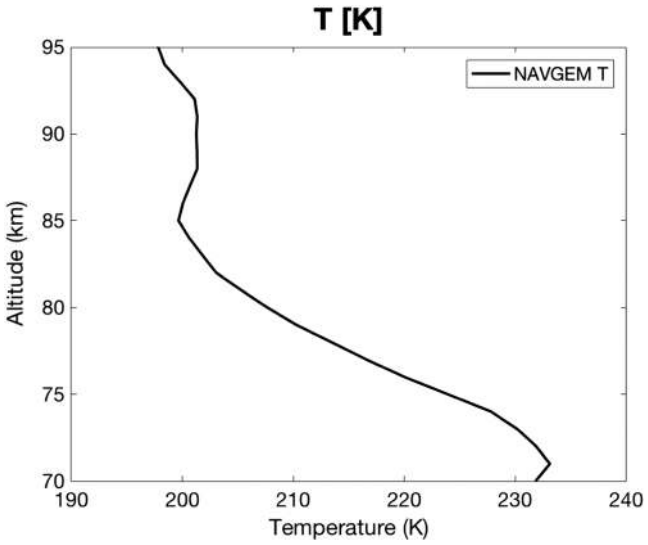

Figure 7. Average NAVGEM temperatures for the duration of RF22 from 6:00 to 9:00 UTC over a 600 km radius circle centered near Mt. Cook.

3.4. MF Spectra Calculations

Assuming hydrostatic motions, the MF per unit mass for a given GW can be calculated as (Bossert et al., 2015; Ern et al., 2004; Fritts et al., 2018),

$$\mathrm{MF} = < u_H' w' > = < \frac{1}{2} \left(\frac{T'}{\overline{T}} \frac{g}{N} \right)^2 \left(\frac{k_H}{m} \right) > \tag{4}$$

where u_H' and w' are the horizontal and vertical wind perturbations of the GW, k_H and m are the horizontal and vertical wavenumbers, and braces denote the mean over the observation segment. While k_H can be obtained from the FFT and corresponding spectral temperature amplitude calculation, m must be calculated using the dispersion relation (Fritts & Alexander, 2003),

$$m^2 = \frac{N^2}{(c - U_H)^2} - \frac{1}{4H^2} - k_H^2 \tag{5}$$

where c is the Earth-relative phase speed assumed to be ~0 m/s for the observed presumed MWs and U_H is the background wind in the direction of the MW horizontal wavenumber vector. Winds for this calculation are obtained from the Kingston meteor radar located on Tasmania, and these have previously been used for analysis in Bossert et al. (2015). Given the small meridional wind magnitudes above 80 km, and the near-zonal propagation direction

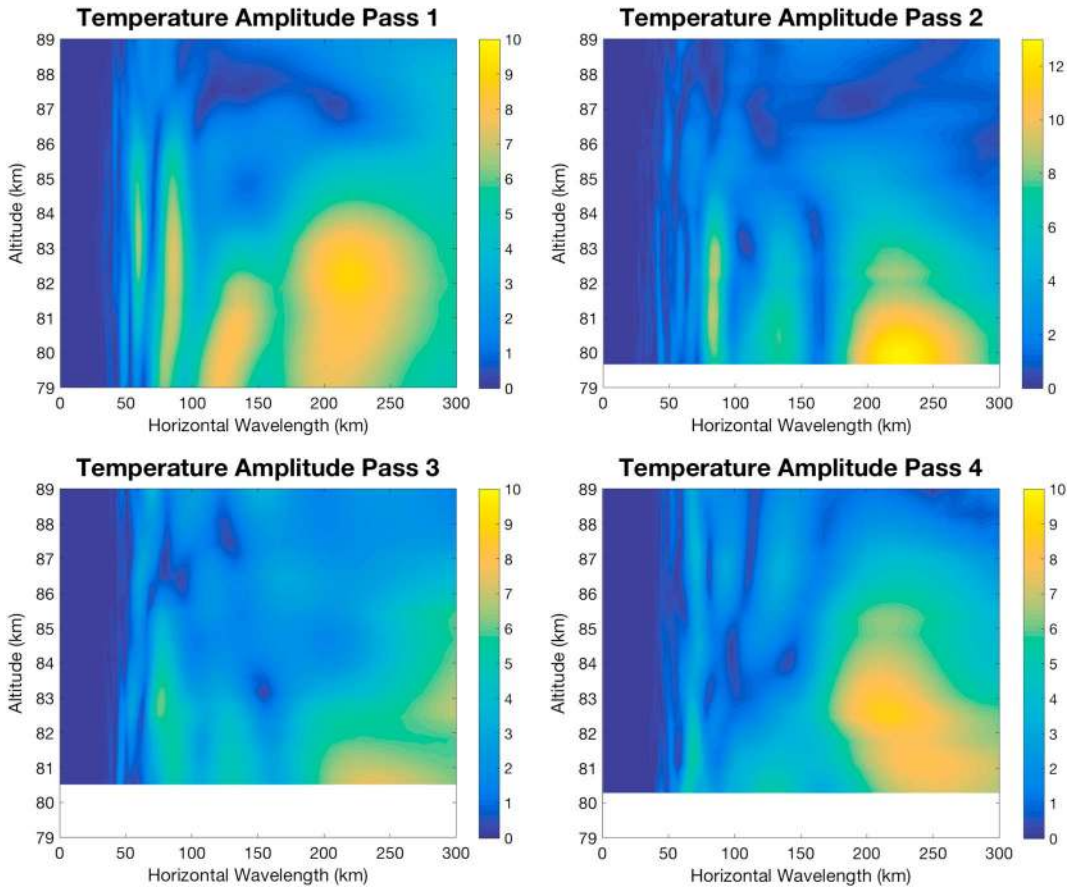

Figure 8. Spectral average T' for each pass calculated from an FFT of the T' shown in Figure 6.

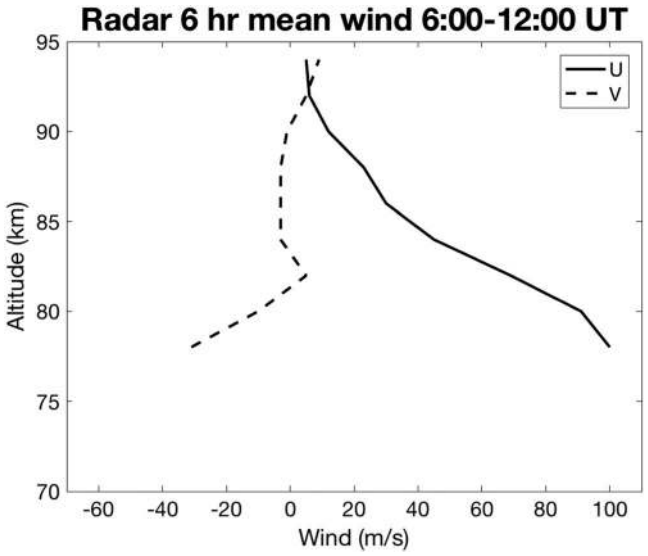

Figure 9. Zonal and Meridional Kingston Meteor radar winds on 13 July 2014 averaged from 6:00 to 12:00UT used in analysis by Bossert et al. (2015).

of the MWs, the zonal winds are used in equation (5) for the calculation of the vertical wavenumber. It is also assumed that the λ_H calculated from the FFT are approximately equal to the λ_H of the actual GWs, although it should be noted that there may be slight offsets in the calculation due to MW orientations slightly off-axis from a zonal propagation. AMTM observations shown in Bossert et al. (2015) demonstrated a nearly zonal orientation of the λ_H ~220 km MW, and other MWs generated under the same forcing conditions would be assumed to have similar orientation. The zonal and meridional winds are shown in Figure 9. The zonal winds imply a critical level near 90 km for stationary MWs. These winds were previously used in Bossert et al. (2015), and an offset time was used to account for tidal influences. It is clear that there is a critical level given the strong decay of MWs leading to 90 km. However, given the distance of the radar observations on Tasmania, the winds used in these calculations provide an estimate and not an exact value and may have associated errors. Given the MW decay in altitude is in agreement with the altitude of the critical level measured by the radar, the radar winds appear to provide a reasonable estimate of background winds with regard to the critical level location. Using equation (4) with the temperature amplitudes given in Figure 6, spectral MF values are obtained over a range of altitudes. The resulting spectral MFs per unit mass are shown in Figure 10. The MF calculations demonstrate the variation of MF between each pass, and between differing λ_H, which is not unexpected given the variability, which can arise in both forcing conditions and atmospheric

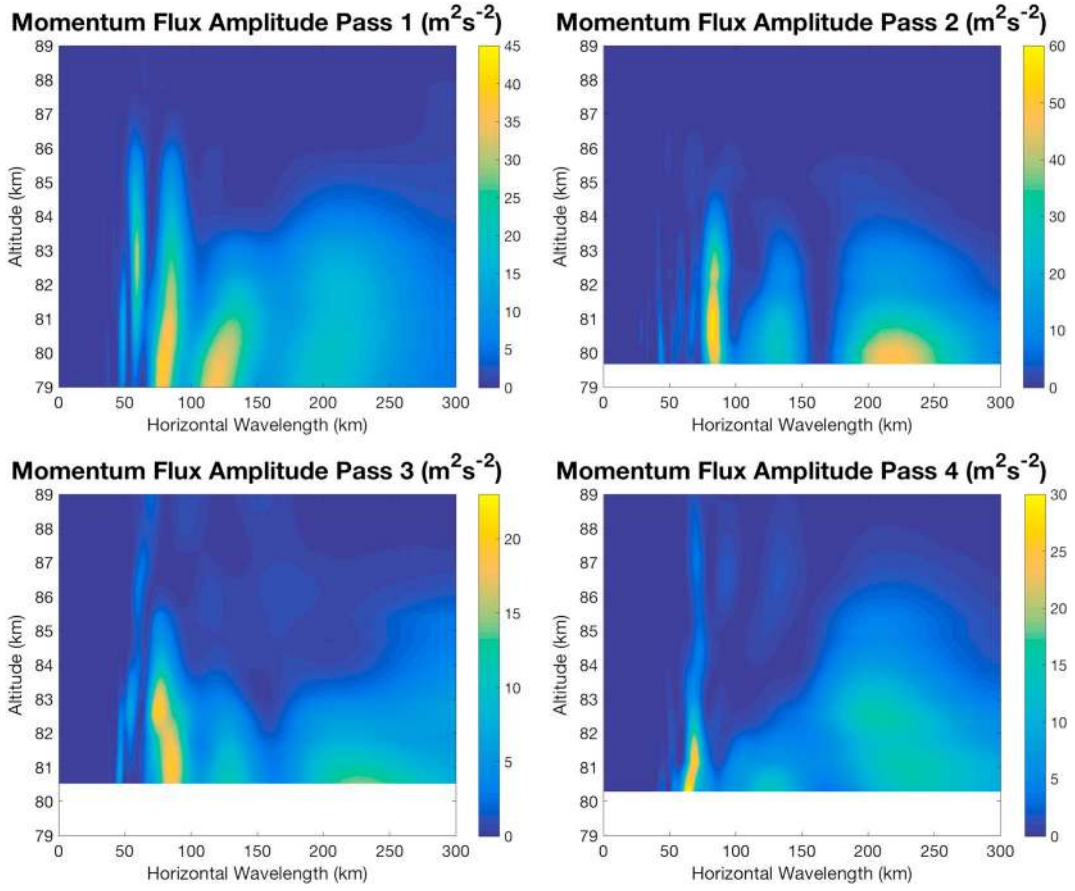

Figure 10. Spectral MF calculated using equation (4), spectral average T' shown in Figure 8, and NAVGEM zonal winds given in Figure 9.

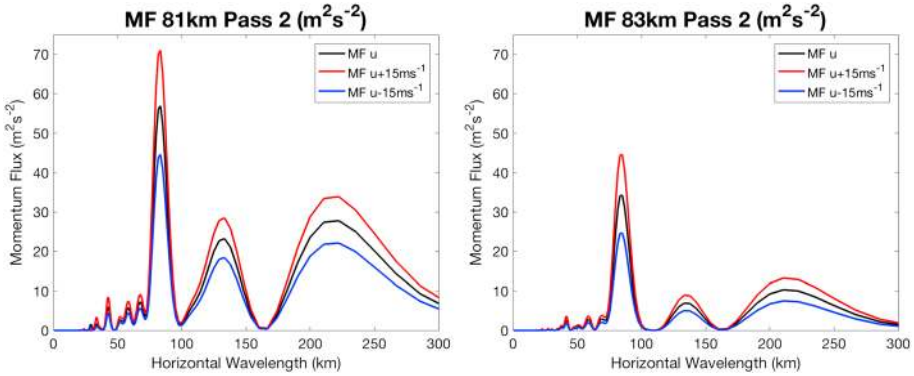

Figure 11. MF calculations for u_H ±15 m/s calculated at 81 and 83 km show error deviations of ~25% for a corresponding wind error of 15 m/s.

propagation conditions over time. It is most notable that the MF quickly decays in altitude, which is expected given the critical level near ~90 km. The first and second GV transects observed the largest MW T' and thus account for the largest MF contributions. The smaller λ_H of 80 and 120 km have MF values of about 35–60 m^2/s^2 on the first and second pass near 81 km, with values significantly decreasing up to 85 km. MF values for these λ_H during the third and fourth passes decrease to values of ~10–25 m^2/s^2 near 80 km. The 220 km λ_H MW had the largest MF contribution during the second pass with MF values of ~50 m^2/s^2 near 80 km. These values are between 10 and 25 m^2/s^2 near 80 km in altitude for the remaining three passes. While horizontal scales of less than 60 km are included in these calculations, these shorter λ_H may have associated ground relative phase speeds, so it is unlikely that the MF calculations associated with these GWs are accurate given the assumed zero ground relative phase speed expected for MWs in the MF calculation. Additionally, as mentioned previously, the winds used in these calculations may have associated errors. To quantify potential errors, the MF was also calculated for winds ±15 m/s. These calculations are shown for the second pass at 81 and 83 km in Figure 11 and demonstrate errors of ~25% for these potential wind deviations from measurements. It should also be noted that T' calculations have larger associated errors lower in altitude due to the varying chemistry at lower altitudes. Additionally, these calculations are an average estimate over the entire flight path, and localized MFs due to stronger phases over the mountains and directly in the lee of the mountains likely have larger associated MFs. Regardless of this, the spectral MF calculations show MF values that are larger than the average background MF values previously measured by radars and satellites, which have ranged from ~1 to 20 m^2/s^2 (Ern et al., 2018; Fritts et al., 2010, 2012; Fritts & Vincent, 1987; Murphy & Vincent, 1993; Nakamura et al., 1993; Reid et al., 1988; Tsuda et al., 1990; Vincent & Reid, 1983; Wang & Fritts, 1990). This finding is qualitatively in good agreement with Hertzog et al. (2012), who showed that MW events are particularly intermittent and strong events can carry very large MFs. Fritts et al. (2018) measured MFs associated with multiscale GW events observed in the OH layer for two separate events, finding maximum MF values for GW packets ranging from ~60 to 940 m^2/s^2. The large MF value in that case was for a short, 10-min period GW that propagated through the OH layer within 45 min. For the 13 July event presented here, MF values were calculated over a sustained period of GW activity over several hours and demonstrate the spectral nature of MWs and varying MF over a range of MWs present in the MLT over New Zealand during this flight.

4. Conclusions and Discussion

The results presented here demonstrate the significant values and variability of MF for a multiscale MW event using a technique for estimating the MF spectra of MWs observed in the sodium density layer during the DEEPWAVE campaign. This technique utilizes observed vertical excursions in sodium mixing ratio isopleths to estimate T' at a given altitude using diagnostic relations derived from parcel relations valid for adiabatic GWs. Na chemistry is shown to have a minor effect on the estimates of T'. The average T' for each wavenumber is then used to assess the mean MF for that GW within the resolved spectrum. Importantly, this necessarily underestimates the total MF when GW amplitudes vary along the flight pass, as it provides an average value.

The results using this T' measurement technique for the 13 July 2014 DEEPWAVE flight demonstrate MFs distributed among a broad range of λ_H along the flight transects. Strongest T' and MF values were observed centered near $\lambda_H \sim 220$, 120, and 80 km, which may be due to multiscale MW generation at the ground level or due to harmonic MW generation from the primary 220 km MW. The observations demonstrate the variability of MWs, which contribute to the vertical transport of horizontal momentum over a GW hot spot. The calculated T' and corresponding MF for MWs within each flight pass spectrum both decrease strongly approaching the critical level near 90 km. However, below this region, MF values are significant over a range of MW λ_H, which are sustained over the period of the several-hour RF.

Acknowledgments
Research reported here was made possible via NSF funding (grants AGS1524598, AGS1338646, AGS1445783, and AGS1151746) acknowledged in GEMS. We acknowledge the generous support of the Chief of Naval Research via the base 6.1, 6.2, and platform support programs. Generation of NAVGEM reanalysis was made possible by the DoD High Performance Computer Modernization Program via grants of computer time at the Navy DoD Supercomputing Resource Center. The Na modeling work was supported by the European Research Council (project 291332-CODITA). Installation and operation of the Kingston radar were supported through Australian Antarctic Science project 4025 and by ATRAD Pty Ltd. We also acknowledge major support by the NCAR/EOL team who made these airborne GV measurements possible. DEEPWAVE data are archived and maintained by NCAR and can be accessed at https://www.eol.ucar.edu/field_projects/deepwave.

References

Acott, P. E., She, C.-Y., Krueger, D. A., Yan, Z.-A., Yuan, T., Yue, J., & Harrell, S. (2011). Observed nocturnal gravity wave variances and zonal momentum flux in mid-latitude mesopause region over Fort Collins, Colorado, USA. *Journal of Atmospheric and Solar-Terrestrial Physics*, *73*(4), 449–456. https://doi.org/10.1016/j.jastp.2010.10.016

Alexander, M. J., Geller, M., McLandress, C., Polavarapu, S., Preusse, P., Sassi, F., et al. (2010). Recent developments in gravity-wave effects in climate models and the global distribution of gravity-wave momentum flux from observations and models. *Quarterly Journal of the Royal Meteorological Society*, *136*, 1103–1124. https://doi.org/10.1002/qj.637

Andreassen, O., Hvidsten, P. O., Fritts, D. C., & Arendt, S. (1998). Vorticity dynamics in a breaking internal gravity wave. Part 1. Initial instability evolution. *Journal of Fluid Mechanics*, *367*, 27–46. https://doi.org/10.1017/S0022112098001645

Badnell, N. R. (2006). Radiative recombination data for modeling dynamics finite-density plasmas. *The Astrophysical Journal Supplement Series*, *167*(2), 334–342. https://doi.org/10.1086/508465

Bossert, K., Fritts, D. C., Pautet, P.-D., Taylor, M. J., Williams, B. P., & Pendelton, W. R. (2014). Investigation of a mesospheric gravity wave ducting event using coordinated sodium lidar and Mesospheric Temperature Mapper measurements at ALOMAR, Norway (69oN). *Journal of Geophysical Research: Atmospheres*, *119*, 9765–9778. https://doi.org/10.1002/2014JD021460

Bossert, K., Fritts, D. C., Pautet, P.-D., Williams, B. P., Taylor, M. J., Kaifler, B., et al. (2015). Momentum flux estimates accompanying multiscale gravity waves over Mount Cook, New Zealand, on 13 July 2014 during the DEEPWAVE campaign. *Journal of Geophysical Research: Atmospheres*, *120*, 9323–9337. https://doi.org/10.1002/2015JD023197

Bossert, K., Kruse, C., Heale, C., Fritts, D. C., Snively, J., Pautet, P.-D., et al. (2017). Secondary gravity wave generation over New Zealand during the DEEPWAVE campaign. *Journal of Geophysical Research: Atmospheres*, *122*, 7834–7850. https://doi.org/10.1002/2016JD026079

Bramberger, M., Dornbrack, A., Bossert, K., Ehard, B., Fritts, D. C., Kaifler, B., et al. (2017). Does strong tropospheric forcing cause large-amplitude mesospheric gravity waves? A DEEPWAVE case study. *Journal of Geophysical Research: Atmospheres*, *122*, 11,422–11,443. https://doi.org/10.1002/2017JD027371

Eckermann, S. D., Broutman, D., Ma, J., Doyle, J. D., Pautet, P.-D., Taylor, M. J., et al. (2016). Dynamics of orographic gravity waves observed in the mesosphere over the Auckland Islands during the Deep Propagating Gravity Wave Experiment (DEEPWAVE). *Journal of the Atmospheric Sciences*, *73*(10), 3855–3876. https://doi.org/10.1175/JAS-D-16-0059.1

Eckermann, S. D., Gibson-Wilde, D. E., & Bacmeister, J. T. (1998). Gravity wave perturbations of minor constituents: A parcel advection methodology. *Journal of the Atmospheric Sciences*, *55*(24), 3521–3539. https://doi.org/10.1175/1520-0469(1998)055<3521:GWPOMC>2.0.CO;2

Eckermann, S. D., Ma, J., Hoppel, K. W., Kuhl, D. D., Allen, D. R., Doyle, J. A., et al. (2018). High-altitude (0–100 km) global atmospheric reanalysis system: Description and application to the 2014 austral winter of the Deep Propagating Gravity-Wave Experiment (DEEPWAVE). *Monthly Weather Review*. https://doi.org/10.1175/MWR-D-17-0386.1

Eckermann, S. D., & Preusse, P. (1999). Global measurements of stratospheric mountain waves from space. *Science*, *286*(5444), 1534–1537. https://doi.org/10.1126/science.286.5444.1534

Ern, M., Preusse, P., Alexander, M. J., & Warner, D. C. (2004). Absolute values of gravity wave momentum flux derived from satellite data. *Journal of Geophysical Research*, *109*, D20103. https://doi.org/10.1029/2004JD004752

Ern, M., Trinh, Q. T., Preusse, P., Gille, J. C., Mlynczak, M. G., Russel, J. M. III, & Riese, M. (2018). GRACILE: A comprehensive climatology of atmospheric gravity wave parameters based on satellite limb soundings. *Earth System Science Data*, *10*(2), 857–892. https://doi.org/10.5194/essd-10-857-2018

Fritts, D. C., & Alexander, M. J. (2003). Gravity wave dynamics and effects in the middle atmosphere. *Reviews of Geophysics*, *41*(1), 1003. https://doi.org/10.1029/2001RG000106

Fritts, D. C., Janches, D., & Hocking, W. K. (2010). Southern Argentina Agile Meteor radar: Initial assessment of gravity wave momentum fluxes. *Journal of Geophysical Research*, *115*, D19123. https://doi.org/10.1029/2010JD013891

Fritts, D. C., Janches, D., Iimura, H., Hocking, W. K., Bageston, J. V., & Leme, N. M. P. (2012). Drake Antarctic Agile Meteor Radar first results: Configuration and comparison of mean and tidal wind and gravity wave momentum flux measurements with Southern Argentina Agile Meteor Radar. *Journal of Geophysical Research*, *117*, D02105. https://doi.org/10.1029/2011JD016651

Fritts, D. C., Smith, R. B., Taylor, M. J., Doyle, J. D., Eckermann, S. D., Dörnbrack, A., et al. (2016). The Deep Propagating GW Experiment (DEEPWAVE): An airborne and ground-based exploration of gravity wave propagating and effects from their sources throughout the lower and middle atmosphere. *Bulletin of the American Meteorological Society*, *97*(3), 425–453. https://doi.org/10.1175/BAMS-D-14-00269.1

Fritts, D. C., & Vincent, R. A. (1987). Mesospheric momentum flux studies at Adelaide, Australia: Observations and a gravity wave/tidal interaction model. *Journal of the Atmospheric Sciences*, *44*(3), 605–619. https://doi.org/10.1175/1520-0469(1987)044<0605:MMFSAA>2.0.CO;2

Fritts, D. C., Vosper, S. B., Williams, B. P., Katrina Bossert, K., Plane, J. M. C., Taylor, M. J., et al. (2018). Large-amplitude mountain waves in the mesosphere accompanying weak cross-mountain flow during DEEPWAVE research flight RF22. *Journal of Geophysical Research: Atmospheres*, *123*. https://doi.org/10.1029/2017JD028250

Garcia, R. R., & Solomon, S. (1985). The effect of breaking gravity waves on the dynamics and chemical composition of the mesosphere andlower thermosphere. *Journal of Geophysical Research*, *90*(D2), 3850–3868. https://doi.org/10.1029/JD090iD02p03850

Gardner, C. S., & Liu, A. Z. (2007). Seasonal variations of the vertical fluxes of heat and horizontal momentum in the mesopause region at Starfire Optical Range, New Mexico. *Journal of Geophysical Research*, *112*, D09113. https://doi.org/10.1029/2005JD006179

Gómez-Martín, J. C., Garraway, S. A., & Plane, J. M. C. (2016). Reaction kinetics of meteoric sodium reservoirs in the upper atmosphere. *The Journal of Physical Chemistry. A*, *120*(9), 1330–1346. https://doi.org/10.1021/acs.jpca.5b00622

Gómez-Martín, J. C., Seaton, C., de Miranda, M. P., & Plane, J. M. C. (2017). The reaction between sodium hydroxide and atomic hydrogen in atmospheric and flame chemistry. *The Journal of Physical Chemistry. A*, *121*(40), 7667–7674. https://doi.org/10.1021/acs.jpca.7b07808

Gong, J., Wu, D. L., & Eckermann, S. D. (2012). Gravity wave variances and propagation derived from AIRS radiances. *Atmospheric Chemistry and Physics*, *12*(4), 1701–1720. https://doi.org/10.5194/acp-12-1701-2012

Heale, C., Bossert, K., Snively, J., Fritts, D. C., Pautet, P.-D., & Taylor, M. J. (2017). Numerical modeling of a multiscale gravity wave event and its airglow signatures over Mount Cook, New Zealand during the DEEPWAVE campaign. *Journal of Geophysical Research: Atmospheres*, *122*, 846–860. https://doi.org/10.1002/2016JD025700

Hertzog, A., Alexander, M., & Plougonven, R. (2012). On the intermittency of gravity wave momentum flux in the stratosphere. *Journal of the Atmospheric Sciences*, *69*(11), 3433–3448. https://doi.org/10.1175/JAS-D-12-09.1

Hoffmann, L., Xue, X., & Alexander, M. J. (2013). A global view of stratospheric gravity wave hotpspots located with Atmospheric Infrared Sounder observations. *Journal of Geophysical Research: Atmospheres*, *118*, 416–434. https://doi.org/10.1029/2012JD18658

Holton, J. R. (1982). The role of gravity wave induced drag and diffusion in the momentum budget of the mesosphere. *Journal of the Atmospheric Sciences*, *39*(4), 791–799. https://doi.org/10.1175/1520-0469(1982)039<0791:TROGWI>2.0.CO;2

Holton, J. R. (1984). The generation of mesospheric planetary waves by zonally asymmetric gravity wave breaking. *Journal of the Atmospheric Sciences*, *41*(23), 3427–3430. https://doi.org/10.1175/1520-0469(1984)041<3427:TGOMPW>2.0.CO;2

Jiang, J. H., Eckermann, S. D., Wu, D. L., Hocke, K., Wang, B., Ma, J., & Zhang, Y. (2005). Seasonal variation of gravity wave sources from satellite observation. *Advances in Space Research*, *35*(11), 1925–1932. https://doi.org/10.1016/j.asr.2005.01.099

Kim, Y.-J., Eckermann, S. D., & Chun, H.-Y. (2003). An overview of the past, present and future of gravity-wave drag parameterization for numerical climate and weather prediction models. *Atmosphere-Ocean*, *41*, 65–98.

Kruse, C. G., Smith, R. B., & Eckermann, S. D. (2016). The mid-latitude lower-stratospheric mountain wave "valve layer.". *Journal of the Atmospheric Sciences*, *73*(12), 5081–5100. https://doi.org/10.1175/JAS-D-16-0173.1

McLandress, C., Alexander, M. J., & Wu, D. L. (2000). Microwave Limb Sounder observations of gravity waves in the stratosphere: A climatology and interpretation. *Journal of Geophysical Research*, *105*(D9), 11,947–11,967. https://doi.org/10.1029/2000JD900097

Murphy, D. J., & Vincent, R. A. (1993). Estimates of momentum flux in the mesosphere and lower thermosphere over Adelaide, Australia, from March 1985 to February 1986. *Journal of Geophysical Research*, *98*(D10), 18,617–18,638. https://doi.org/10.1029/93JD01861

Nakamura, T., Tsuda, T., Yamamoto, M., Fukao, S., & Kato, S. (1993). Characteristics of gravity waves in the mesosphere observed with the middle and upper atmosphere radar: 1. Momentum flux. *Journal of Geophysical Research*, *98*(D5), 8899–8910. https://doi.org/10.1029/92JD02978

Pautet, P.-D., Taylor, M. J., Fritts, D. C., Bossert, K., Williams, B. P., Broutman, D., et al. (2016). Large amplitude mesospheric response to an orographic wave generated over the Southern Ocean Auckland Islands (50.7°S) during the DEEPWAVE project. *Journal of Geophysical Research: Atmospheres*, *121*, 1431–1441. https://doi.org/10.1002/2015JD024336

Plane, J. M. C. (2004). A time-resolved model of the mesospheric Na layer: Constraints on the meteor input function. *Atmospheric Chemistry and Physics*, *4*(3), 627–638. https://doi.org/10.5194/acp-4-627-2004

Reid, I. M., Ruster, R., Czechowsky, P., & Schmidt, G. (1988). VHF radar measurements of momentum flux in the summer polar mesosphere over Andenes (69°N, 16°E), Norway. *Geophysical Research Letters*, *15*(11), 1263–1266. https://doi.org/10.1029/GL015i011p01263

Shelton, J. D., Gardner, C. S., & Sechrist, C. F. Jr. (1980). Density response of the mesospheric sodium layer to gravity wave perturbations. *Geophysical Research Letters*, *7*(12), 1069–1072. https://doi.org/10.1029/GL007i012p01069

Smith, R., & Kruse, C. (2017). Broad spectrum mountain waves. *Journal of the Atmospheric Sciences*, *74*(5), 1381–1402. https://doi.org/10.1175/JAS-D-16-0297.1

Swenson, G. R., & Gardner, C. S. (1998). Analytical models for the responses of the mesospheric OH* and Na layers to atmospheric gravity waves. *Journal of Geophysical Research*, *103*(D6), 6271–6294. https://doi.org/10.1029/97JD02985

Tsuda, T., Murayama, Y., Yamamoto, M., Kato, S., & Fukao, S. (1990). Seasonal variation of momentum flux in the mesosphere observed with the MU radar. *Geophysical Research Letters*, *17*(6), 725–728. https://doi.org/10.1029/GL017i006p00725

Vincent, R. A., & Reid, I. M. (1983). HF Doppler measurements of mesospheric momentum fluxes. *Journal of the Atmospheric Sciences*, *40*(5), 1321–1333. https://doi.org/10.1175/1520-0469(1983)040<1321:HDMOMG>2.0.CO;2

Wang, D.-Y., & Fritts, D. C. (1990). Mesospheric momentum fluxes observed by the MST radar at Poker Flat, Alaska. *Journal of the Atmospheric Sciences*, *47*(12), 1512–1521. https://doi.org/10.1175/1520-0469(1990)047<1512:MMFOBT>2.0.CO;2

Wu, D. L., Preusse, P., Eckermann, S. D., Jiang, J. H., de la Torre Juarez, M., Coy, L., & Wang, D. Y. (2006). Remote sounding of atmospheric gravity waves with satellite limb and nadir techniques. *Advances in Space Research*, *37*(12), 2269–2277. https://doi.org/10.1016/j.asr.2005.07.031